INT. J. NUM. METH. HEAT FLUID FLOW, VOL. 2, 155–169 (1992)

FINITE ELEMENT ANALYSIS OF STIRRING INDUCED BY AN ALTERNATING MAGNETIC FIELD

M. BERELOWITZ AND P. BAR-YOSEPH

Computational Mechanics Laboratory, Faculty of Mechanical Engineering, Technion—Israel Institute of Technology, Haifa 32000, Israel

ABSTRACT

The numerical investigation into the stirring induced by an alternating magnetic field, applied in the axial direction of a closed axisymmetric container of conducting fluid, is presented. The interaction between the azimuthal current and magnetic field results in Lorentz forces in the meridional plane which induce the fluid flow. The magnetic Reynolds number is assumed to be smaller than the frequency magnetic Reynolds number. The electromagnetic equations are thus decoupled from the fluid flow equations. The electromagnetic field is first solved, and the body forces determined from this are introduced into the Navier–Stokes equations. With the flow field known, the quality of mixing is determined by solving the tracer dispersion equation. The finite element method based on a Galerkin formulation is used for the solution of the equations. Three cases are examined: a finite length cylinder, a finite length cylinder with rounded corners and a sphere. In general, two vortices are formed, the equatorial vortex closest to the equator and the end vortex at the closed end. Results show that the introduction of the rounded corner increases the size and strength of the end vortex with the opposite effect on the equatorial vortex. Of the three frequency magnetic Reynolds numbers considered ($R_\omega = 30$, 100 and 800), $R_\omega = 100$ results in the best mixing for all cases. Rounding the corner of the cylinder only results in a definite improvement of mixing at $R_\omega = 800$. The sphere results in even better mixing than this at $R_\omega = 800$, but is worse than the first two geometries for $R_\omega = 30$ and 100 when the interaction parameter is large.

KEY WORDS Galerkin formulation Alternating magnetic fields Stirring

INTRODUCTION

During the past decade there has been a growing interest in the improvement of ladle metallurgy for the finishing treatment of molten steel. Some form of ladle metallurgy step, such as argon stirring in order to achieve homogenization, has become an established component of the overall steel making sequence.

In general, the operation of typical ladle metallurgy systems involves the agitation of melts that may range from 5 to 250 tons in size, using injected-gas streams, vacuum-driven circulation systems or electromagnetic force fields. In addition to homogenization, agitation also causes chemical and physical changes. For mixing problems in general, theoretical[1–3], experimental[1–4,7] and numerical[8] studies have been undertaken. For this, a variety of different schemes have been used in attempting to quantify the mixing of the resultant flow fields.

For the stirring of conducting fluids by magnetic fields, various theoretical studies[9–11] have been undertaken. These, however, have been rather limited due to the complicated nature of the equations. Experimental investigations have thus been crucial to gaining an understanding of the phenomena and processes involved[7,12–17]. Owing, to the inherent problems of experiments with liquid metals and with the onset of computing power, an increasing use is being made of

0961-5539/92/020155-15$2.00

Received March 1991
Revised December 1991

the mathematical modelling of these types of problems. With respect to the present problem, numerous works using the finite difference method have been undertaken[8,12,14,16–19]. While the finite element method has successfully been employed for other MHD problems[20–22], to the best of our knowledge, it has not yet been used for the present type of problem.

The studies on the stirring induced by alternating magnetic fields parallel to the axis of symmetry can be classified as follows: (i) the inclusion or exclusion of flow induced currents which renders the magnetic field equations and fluid flow equations coupled or uncoupled respectively; (ii) a finite length coil or a uniform external magnetic field of an infinite coil; (iii) an open or closed crucible, where the former can be considered to have a flat free surface or the cupola effect on the free surface can be determined; and (iv) laminar flow or turbulent flow, with various possible turbulent models.

So while a fair amount of work has been done in this field, the only geometrical consideration other than length to radius ratio of the cylinder has been the determination of the cupola effect of the free surface. However, in practice the corner of the crucible is often rounded because of the severe erosion which occurs there. To the best of our knowledge, no previous work has been done on the above problem which employs the finite element method for the entire problem of magnetic field solution, flow determination and mixing. For this reason, the effect of geometry on the resultant flow and mixing has also not been investigated. It is to this problem of the effect of geometry on the mixing, that the present research addresses itself.

THEORETICAL DEVELOPMENT

The problem considered for study is the stirring induced in electrically conducting fluids by alternating magnetic fields. The effect of crucible geometry on the flow patterns and on the mixing which results from this, is investigated. Specifically, the study is confined to closed axisymmetric arbitrarily shaped containers. The magnetic field is derived from an infinite length coil wound around the container and the magnetic field at infinity is thus parallel to the axis of the container. The particular geometries chosen for investigation exhibit plane symmetry.

Fluid equations

The Navier–Stokes equations incorporating the electromagnetic body force are used. The flow can be assumed to be steady, laminar and isothermal[18]. Under these assumptions, the governing fluid equations in dimensionless form are:

$$(\mathbf{V}_a \cdot \nabla)\mathbf{V}_a = -\nabla p + \frac{1}{R}\nabla^2 \mathbf{V}_a + \mathbf{J} \times \mathbf{B} \tag{1}$$

$$\nabla \cdot \mathbf{V}_a = 0 \tag{2}$$

where R is the interaction parameter:

$$R := \frac{V_{AI} L}{\nu} \propto \frac{\text{electromagnetic forces}}{\text{viscous forces}} \tag{3}$$

V_{AI} is the Alfven speed of propagation of a magnetohydrodynamic wave:

$$V_{AI} := \frac{B_0}{\sqrt{\mu\rho}} \tag{4}$$

L is a characteristic length scale, B_0 is the strength of the external applied magnetic field, μ is the magnetic permeability of free space, $\mathbf{V}_a$ is the velocity vector normalized with respect to V_{AI}, ν is the kinematic viscosity, $\mathbf{J}$ is the current density, ρ is the fluid density, and $\mathbf{B}$ is the magnetic flux density.

The axisymmetric form of the fluid equations are used, i.e. polar coordinates (r, θ, z). For the problem under consideration, no body forces are present in the azimuthal direction, so the azimuthal velocity component is set to zero.

Electromagnetic equations

Maxwell's equations for magnetohydrodynamic flows together with Faraday's and Ohm's laws are used[23].

The magnetic vector potential **A** is defined by:

$$\nabla \times \mathbf{A} = \mathbf{B} \tag{5}$$

The result of this is to transform the problem of solving for two non-zero scalar components of the magnetic field **B** to a problem of solving for a single non-zero scalar component of the magnetic vector potential **A**. Numerically, this has the advantage of reducing the number of degrees of freedom by half.

As customary[24], the following additional constraint is enforced:

$$\nabla \cdot \mathbf{A} = 0 \tag{6}$$

The dimensionless form of the magnetic vector potential equation can then be expressed as[18,25]:

$$-\nabla^2 \mathbf{A} = -R_\omega \frac{\partial \mathbf{A}}{\partial t} + R_m \mathbf{V} \times (\nabla \times \mathbf{A}) = \mathbf{J} \tag{7}$$

where R_ω is the frequency magnetic Reynolds number

$$R_\omega := \mu\sigma\omega L^2 \tag{8}$$

where $\omega = 2\pi f$ and f is the applied frequency of the alternating magnetic field, and R_m is the magnetic Reynolds number:

$$R_m := \mu\sigma V_0 L \propto \frac{\text{induced magnetic field strength}}{\text{imposed magnetic field strength}} \tag{9}$$

where the velocity vector **V** is normalized with respect to V_0, a typical velocity scale of the motion, time is normalized with respect to ω^{-1} and σ is the electrical conductivity of the fluid.

Referring to (7), R_m is assumed to be much smaller than R_ω, which means that the electric currents induced by the motion of the fluid particles across the lines of force (the term containing the R_m) will be negligible compared to the electric currents induced by the pulsation of the applied magnetic field (the term containing the R_ω). Therefore, (7) reduces to:

$$-\nabla^2 \mathbf{A} = -R_\omega \frac{\partial \mathbf{A}}{\partial t} = \mathbf{J} \tag{10}$$

Thus, by limiting the study to $R_\omega \gg R_m$ the electromagnetic equations are decoupled from the fluid equations.

Assuming axisymmetry and the magnetic field applied parallel to the axis, the equations are expressed in polar coordinates (r, θ, z) so that (10) reduces to a single equation governing the one-component vector potential, i.e.

$$\mathbf{A} = A' \hat{\mathbf{e}}_\theta \tag{11}$$

If the applied magnetic field is a sinusoidal function of time, then a solution for A' of the form:

$$A' = \Re(\hat{A} e^{it}) \tag{12}$$

where

$$\begin{aligned} \hat{A} &= A_m e^{i\phi} \\ &= a + ib \end{aligned} \tag{13}$$

can be sought. The vector potential $\hat{A}$ is thus described by its real and imaginary parts a and b or by its phase ϕ and amplitude A_m, which are both functions of the coordinates (r, z). Equation (10) thus becomes,

$$\nabla^2 \hat{A} = iR_\omega \hat{A} \tag{14}$$

The boundary conditions are:

The magnetic field is assumed to be uniform at infinity, and so $\hat{A} \approx r$ at infinity. In terms of a and b, this means that, on the axis, i.e. at $r=0$: $a=0$ and $b=0$ and at the boundary far from the conducting medium: $a=r$ and $b=0$.

The magnetic field must be continuous across the boundary. Thus (5) requires the derivatives of $\hat{A}$ to be continuous across boundaries between different media.

The body force term can be calculated from the solution of the magnetic vector potential solution for the Navier–Stokes equations. The body force term is given by:

$$\begin{aligned} \mathbf{J} \times \mathbf{B} &= -R_\omega \frac{\partial \mathbf{A}}{\partial t} \times \mathbf{B} \\ &= (R_\omega A_m \sin(t+\phi)\hat{\mathbf{e}}_\theta) \times \nabla \times (A_m \cos(t+\phi)\hat{\mathbf{e}}_\theta) \end{aligned} \tag{15}$$

Moreau[26] showed that the time-period variation of the force around the mean value has little hydrodynamical importance. Therefore, with the inertial response of the fluid to the periodic part of the Lorentz force neglected, the mean value of the force field over a period is used. The driving force is therefore defined as:

$$\begin{aligned} \langle \mathbf{J} \times \mathbf{B} \rangle &:= \frac{1}{T} \int_0^T \mathbf{J} \times \mathbf{B} \, d\tau \\ &= -\frac{R_\omega}{2} A_m^2 \nabla \phi \end{aligned} \tag{16}$$

where $\langle\ \rangle$ denotes the time average, and $T = 2\pi/\omega$. Once solved, the assumption that $R_\omega \gg R_m$ can be checked.

Dispersion of tracers

With the fluid flow field is known, the dispersion of a tracer, which may be used to characterize the mixing rates, may be represented in dimensionless form as:

$$\frac{\partial C}{\partial t} + \mathbf{V}_a \cdot \nabla C = \frac{1}{Pe} \nabla^2 C \tag{17}$$

where C is the tracer concentration, Pe is the Peclet number defined by:

$$Pe := \frac{V_{Al} L}{\alpha} \propto \frac{\text{convectivity transport rate}}{\text{diffusivity transport rate}} \tag{18}$$

and α is the tracer diffusivity.

FINITE ELEMENT FORMULATION

To solve the Navier–Stokes equations, (1), we use the penalty method. The discrete weak formulation is then given as[27]:

$$c(\mathbf{u}_\varepsilon^h, \mathbf{u}_\varepsilon^h, \mathbf{v}^h) + R^{-1} d(\mathbf{u}_\varepsilon^h, \mathbf{v}^h) + \varepsilon^{-1} (\nabla \cdot \mathbf{u}_\varepsilon^h, \nabla \cdot \mathbf{v}^h) = (\mathbf{f}, \mathbf{v}^h) \tag{19}$$

where (β, γ) denotes the usual $[L_2(\Omega)]^n$, $(n=1,2)$, inner product with β and γ denoting generic

scalar or vector functions, and

$$d(\beta,\gamma)=\int_\Omega \nabla\beta\cdot\nabla\gamma\,d\Omega$$

$$c(\beta,\beta,\gamma)=\int_\Omega (\beta\cdot\nabla\beta)\gamma\,d\Omega$$

are the bilinear and trilinear forms of the diffusive and convective terms, respectively and ε is a small positive number, the penalty parameter.

Choosing the same finite element subspace as used for the velocity vectors in the fluid flow equations, the weak formulation of the magnetic vector potential is:

$$d(\hat{A}^h,w^h)-iR_\omega(\hat{A}^h,w^h)=0 \tag{20}$$

The electromagnetic matrix equations which result from the formulation are linear while those of the fluid flow problem are non-linear due to the convective terms.

For the flow problem, a solution by continuation-Newton algorithms is used to trace the branches in the parameter space along which steady flow states lie. In this study, a zeroth-order continuation (incremental 'loading') in R with step size control follow the solution branch from a given unique solution state. The interaction parameter R is incremented until a solution at the required interaction parameter is attained. The advantage of this technique is that solutions are available for a range of interaction parameters. At each continuation step, a non-linear equation set is solved by a Newton iteration and the approximation to the solution at each iteration is found by a modified frontal solver[28], for an in-core solution of large, sparse, non-symmetric systems of the set of linearized equations. Iterations at each load step are performed until convergence is achieved.

The penalty parameter ε was typically set to 10^{-6}. The flow solutions obtained were found to vary insignificantly for variations in ε of several orders of magnitude.

Quantifying mixing

The tracer dispersion problem was solved by the classical standard Galerkin method[29] used for convective–diffusive type problems. Explicit time integration, the Euler method, was used for the time marching procedure. Identical meshes as used for the flow equations were used for these as well, with biquadratic elements also employed. The solution obtained from the flow problem was supplied as the steady flow field for the tracer dispersion equation. At $t=0$, all the tracer was concentrated in a small area. Numerically this was done by setting the initial tracer concentration at all the nodes of one particular element to 1.0 and setting all the other nodes initially to zero. The boundary conditions were zero flux of tracer at all the boundaries. The value of Pe was set at 1000 to ensure the dominance of convectivity transport rate over diffusivity transport rate of tracer. Constant steps of one dimensionless unit of time were used for the numerical time stepping procedure. This was checked with smaller time steps and the solutions of the quality of mixing were found to deviate insignificantly from these. In all cases the problems were run for 100 dimensionless units of time and then a mixing index (MI) was calculated from the resultant tracer distribution to quantify the mixing. The MI we define as the integral over the volume of the deviation of the tracer concentration from the average tracer concentration normalized with respect to the total tracer quantity, i.e.

$$\mathrm{MI}=\frac{\sum_e \int_{\Omega^e} |C^h-\bar{C}|\,d\Omega^e}{\bar{C}V(\Omega)} \tag{21}$$

where

$$\bar{C}=\frac{\sum_{e}\int_{\Omega^e} C^h \, d\Omega^e}{V(\Omega)} \tag{22}$$

and $V(\Omega)$ is the volume of the domain.

Geometrical model

The following three geometries were considered for investigation of the mixing problem:

(1) a cylinder with radius and half length equal to 1.0;
(2) a cylinder the same as the one above but with a rounded corner. The radius of curvature of the corner was 0.3;
(3) a sphere of radius 1.0. While a closed spherical container is almost certainly not a technologically practical geometry, it represents the extreme extrapolation of rounding the corner of the above cylinders.

In all three cases, the containers were closed and thus exhibited plane symmetry about the equatorial plane. The magnetic field from an infinite length coil was applied. The computational boundaries were set at $r=0,2$ and $z=0,3$ in all the cases. A representative example of this type of problem with the magnetic vector potential boundary conditions and with the fluid flow boundary conditions is shown schematically in *Figure 1*.

In all cases, biquadratic isoparametric elements were used for the electromagnetic field problem as well as for the flow problem. For the magnetic field problem, the part of the mesh representing the conducting fluid was identical to the mesh of the fluid flow problem. This facilitated the transfer of the body force solution from the electromagnetic problem to the flow problem.

Figure 2 shows the meshes corresponding to the fluid flow field for the three cases considered. The elements marked A correspond to the elements which were given the initial tracer concentration for the tracer dispersion problem. Other elements were also used for the initial location of tracer concentration in order to investigate the effect of this on the resultant determination of the mixing index.

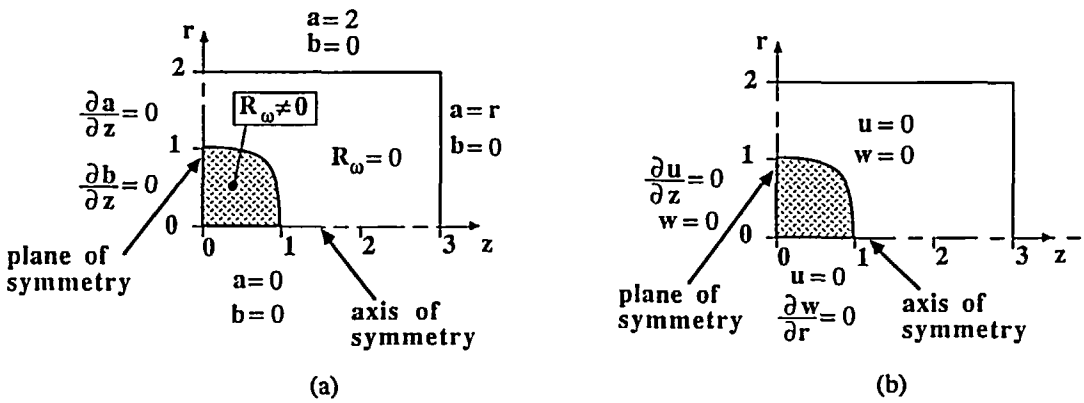

Figure 1 A typical problem showing (a) the electromagnetic potential boundary conditions and (b) the flow boundary conditions

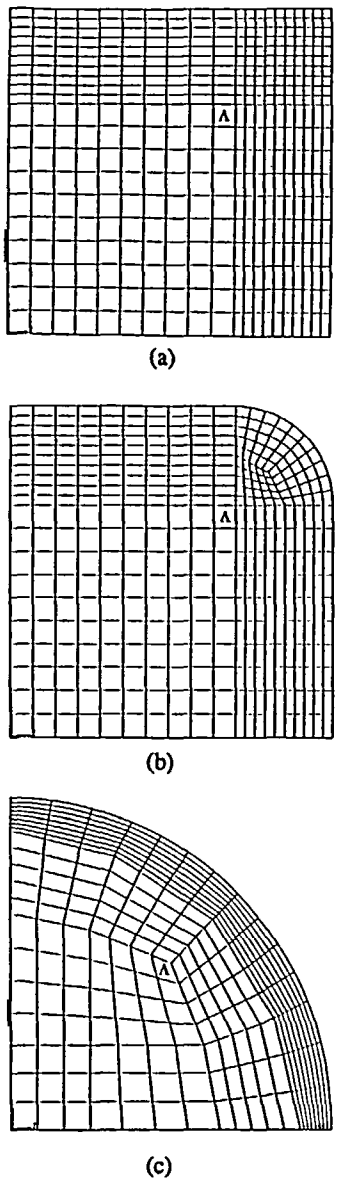

Figure 2 Meshes used for the fluid problem for the three cases considered. (a) The cylinder with the sharp corner, (b) the cylinder with the rounded corner and (c) the sphere

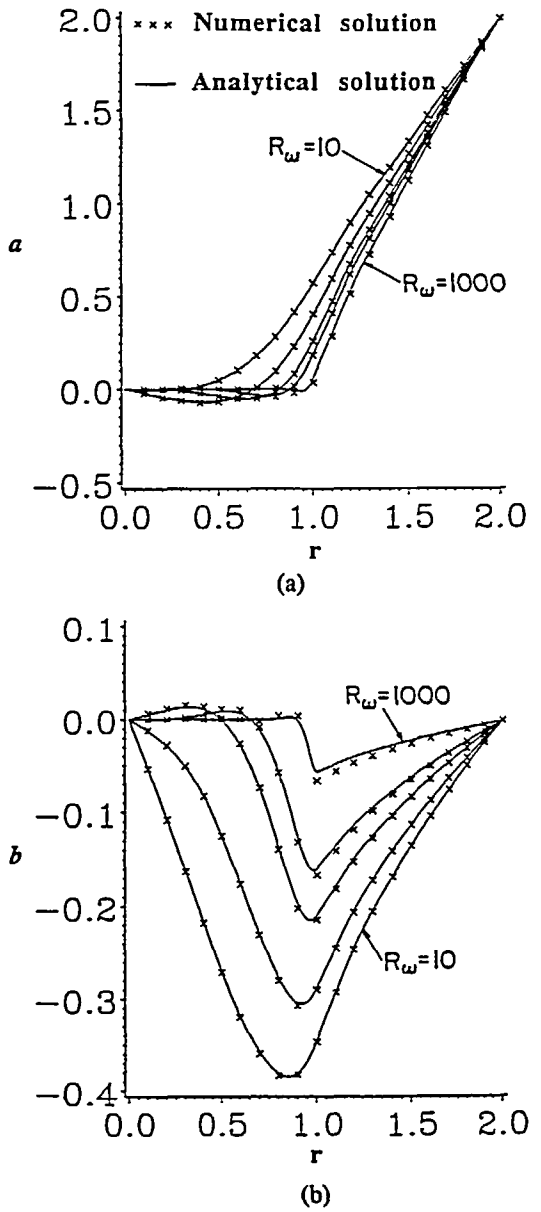

Figure 3 Numerical and exact solution of the magnetic vector potential for an infinite cylinder. $R_\omega = 10$, 20, 50, 100 and 1000. (a) The real part a, and (b) the imaginary part b

RESULTS AND DISCUSSION

Magnetic field around an infinitely long cylinder

A comparison between the numerical solution and the exact solution[25] of the magnetic field around an infinitely long cylinder is shown in *Figure 3*. The cylinder has a radius of 1.0 and the external magnetic field is specified at a radius of 2.0. The numerical solution was obtained using

20 equal bilinear elements in the radial direction with zero derivatives imposed in the axial direction. As can be seen, the numerical results are in excellent agreement with the exact solution. As expected, the deviation from the exact solution is largest at the largest value of R_ω where the skin depth is the smallest.

Three geometries considered

For each of the three different geometries, the computations were performed for three different value of R_ω, viz., $R_\omega = 30$, 100 and 800. The changes which occur for increasing R_ω are as expected from previous researchers[18]. The depth of penetration of the lines of equal a become smaller for larger R_ω and the medium change is highly noticeable in the solution of b, viz. as R_ω increases the gradients of b become shallower everywhere except in the vicinity of the medium change. Typical results which show the influence of the different geometries on the solutions of a and b are shown in *Figure 4*. The force fields computed from the solutions also follow the known trend, i.e., as R_ω increases the magnitude of the maximum force increases and the force field becomes concentrated in the thin skin layer.

A comparison of the magnetic vector potential solution *versus* the radius r at the equator for the cylinder and sphere to the exact solution for an infinite cylinder of radius 1.0 with the same external applied magnetic field is shown in *Figures 5* and *6*. *Figure 5* is for the case of $R_\omega = 30$ and *Figure 6* is for $R_\omega = 800$. As can be seen the deviation is greatest for the sphere as one would expect, and is greater for smaller R_ω, which could be a result of the greater penetration depth and hence effected to a greater extent by the geometry.

Figure 7 shows the resulting flow streamlines for $R_\omega = 800$ and $R = 1600$ for the cylinder with the rounded corner. As can be seen two toroidal vortices are present. The vortex closest to the plane of symmetry at the equator, the equatorial vortex, rotates clockwise. The other vortex,

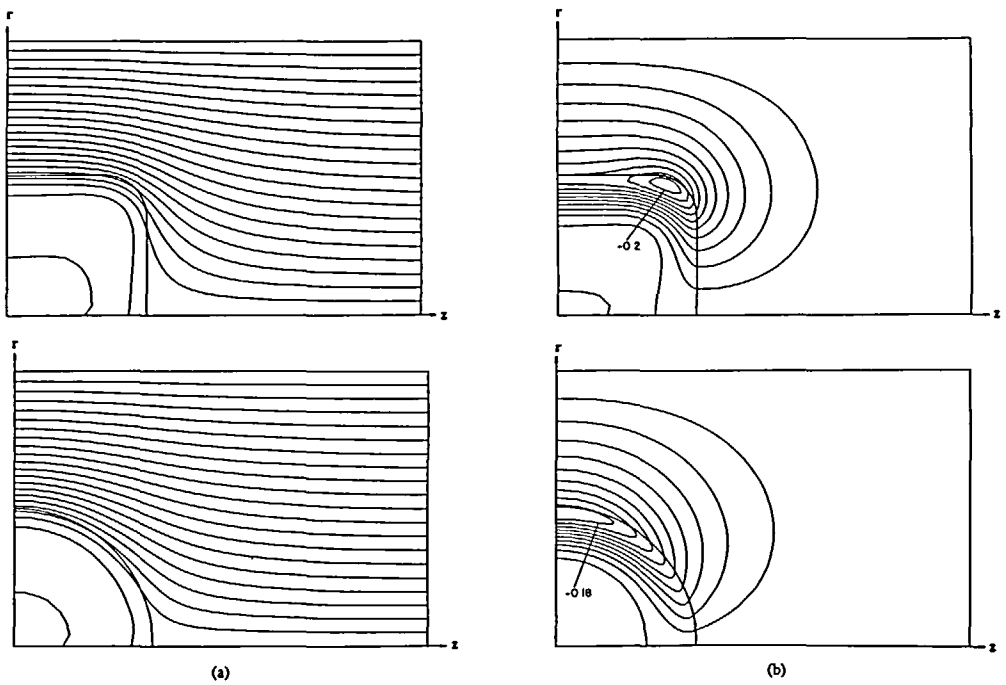

Figure 4 Magnetic vector potential around the cylinder with the rounded corner and the sphere for $R_\omega = 100$. (a) The real part a in equal increments of 0.1, and (b) the imaginary part b in equal increments of 0.02

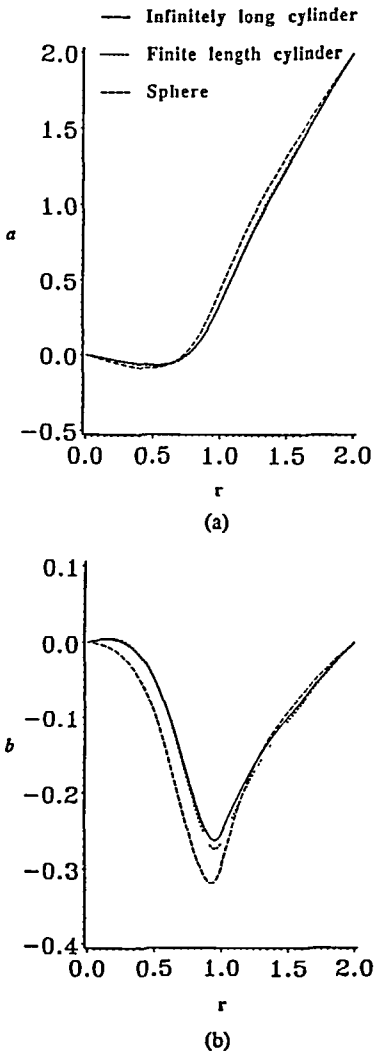

Figure 5 Comparison of the equatorial solution of the magnetic vector potential for the cylinder and sphere to the exact solution for an infinite cylinder for $R_\omega = 30$. (a) The real part a, and (b) the imaginary part b

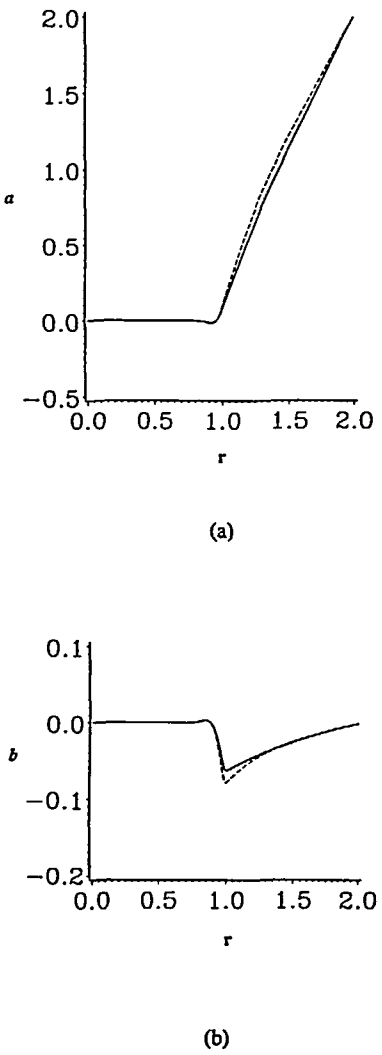

Figure 6 Comparison of the equatorial solution of the magnetic vector potential for the cylinder and sphere to the exact solution for an infinite cylinder for $R_\omega = 800$. (a) The real part a, and (b) the imaginary part b

the end vortex, rotates counter-clockwise. *Figure 8* shows the flow streamlines for the same geometry but with $R_\omega = 100$ and $R = 1600$ while the result for $R_\omega = 800$ and $R = 200$ is shown in *Figure 9*. From these we can see the trends found for the resulting flows with respect to changes in the parameters R_ω and R which are in agreement with those of previous researchers[13,16,18] viz., as R or R_ω increase, the equatorial vortex grows in size at the expense of the end vortex.

The effect of changes in geometry can be seen by comparing *Figures 7*, *10* and *11* which show the resulting streamlines for $R_\omega = 800$ and $R = 1600$ for the three geometries considered. In the sphere, with only one vortex present, that vortex is analogous to the end vortices of the other two geometries. A comparison of the maximum value of the stream function of the end vortices for the various geometries and operating parameters is shown in *Table 1*.

In comparing the flow results, it can be seen that the maximum value of the streamfunction

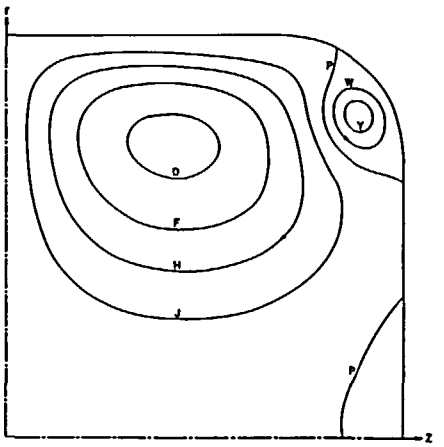

Figure 7 Flow streamlines in the cylinder with a rounded corner for $R_\omega = 800$ and $R = 1600$. The streamfunction values for this and all the flow Figures which follow are given in the Appendix

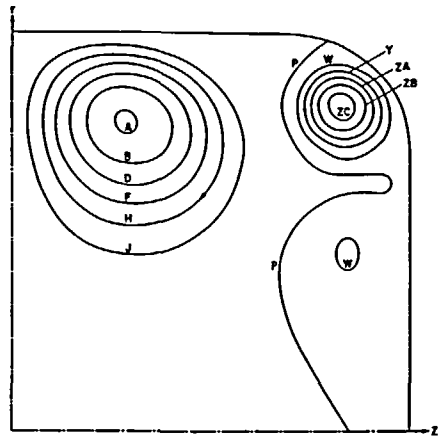

Figure 8 Flow streamlines in the cylinder with a rounded corner for $R_\omega = 100$ and $R = 1600$

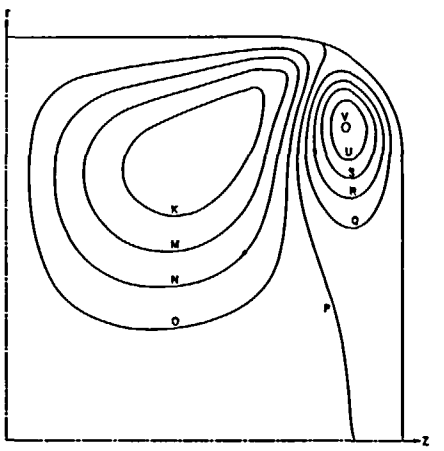

Figure 9 Flow streamlines in the cylinder with a rounded corner for $R_\omega = 800$ and $R = 200$

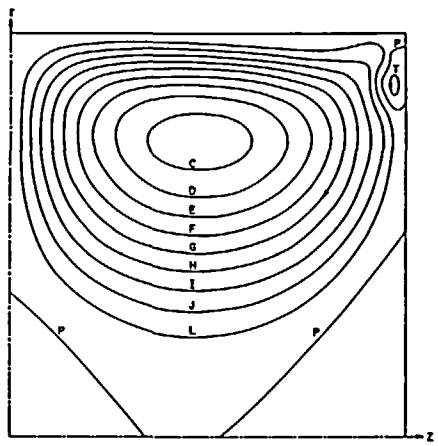

Figure 10 Flow streamlines in the cylinder for $R_\omega = 800$ and $R = 1600$

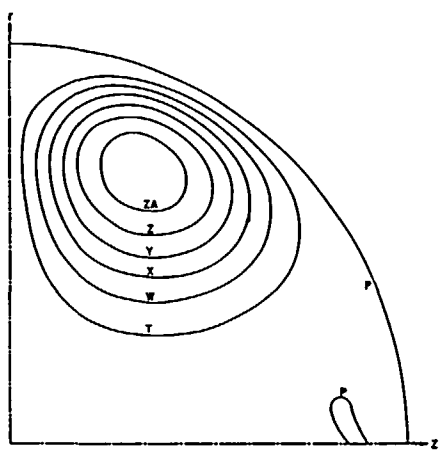

Figure 11 Flow streamlines in the sphere for $R_\omega = 800$ and $R = 1600$

Table 1 Comparison of the maximum streamfunction value of the end vortex for the different cases and parameters

	Cylinder R_ω			Rounded corner R_ω			Sphere R_ω		
R	30	100	800	30	100	800	30	100	800
200	0.069	0.036	0.015	0.102	0.079	0.030	0.143	0.101	0.021
400	0.10	0 053	0.016	0.158	0.126	0.051	0.215	0.17	0.041
800	0.15	0.089	0.023	0.219	0.19	0.080	0.214	0.2	0.080
1197								0.18	
1560							0.224		
1600	0.16	0.109	0.031	0.227	0.22	0.105			0.136
3140									0.188

Table 2 Comparison of the maximum absolute stream function value of the equatorial vortex for the cylinder and the cylinder with the rounded corner

	Cylinder R_ω			Cylinder with rounded corner R_ω		
R	30	100	800	30	100	800
200	−0.06	−0.10	−0.04	−0.04	−0.09	−0.03
400	−0.10	−0.17	−0.09	−0.08	−0.15	−0.06
800	−0.15	−0.22	−0.14	−0.14	−0.21	−0.11
1600	−0.15	−0.24	−0.19	−0.13	−0.24	−0.17

of the end vortex decreases as R_ω increases and increases for greater rounding of the corner (except in the sphere for high value of R).

For the equatorial vortex, a different phenomenon is present. Here, the vortex has a maximum absolute streamfunction value for $R_\omega = 100$ but decreases with the rounding of the corner. Typical values are shown in *Table 2* which gives the values of the stream function of the eye of the equatorial vortex for the cylinder and the cylinder with the rounded corner.

Regarding the solution strategy, a typical run was as follows: for the cylinder with the sharp corner, the magnetic vector potential was solved for $R_\omega = 100$. The flow equations were then solved by incremental loading of R. The Stokes equations were solved for the first iteration of the first value of R. Thereafter, the Newton–Raphson scheme was used for solving the equations. When convergence was attained, R was incremented. For this particular parameter set, increments of 100 up to $R = 800$ were possible, with the typical quadratic convergence associated with the scheme obtained. Thereafter, increments as small as 20 were necessary, but at $R = 1700$ increments of 100 were once again possible up to $R = 2300$.

The convergence characteristics of the scheme were also found to be mesh dependent. With the converged solution at the highest value of R obtained, increments of as little as 1 could not yield the next solution. Non-convergence could have several meanings. It could be that a higher order continuation method is necessary due to a bifurcation of the solution. Alternatively, it could simply be a manifestation of the non-existence of a steady or laminar solution.

A comparison of the geometrical effect on the maximum velocity, $V_{max} = \max(\sqrt{u^{h^2} + w^{h^2}})$, obtained in the flow field for fixed values of R_ω and R is shown in *Figure 12*. As can be seen in the first graph, for $R_\omega = 30$, the sphere has the highest V_{max} while the cylinder has the lowest. At $R_\omega = 100$, the cylinder has the lowest V_{max}, but the rounded corner cylinder has the greatest V_{max} and at $R_\omega = 800$, the sphere has the lowest V_{max} with the rounded corner cylinder having the greatest for $R > 900$. The results thus show a clear influence of geometry on the maximum velocity and flow field and demonstrate the ability of being able to choose between geometry, R_ω and R to obtain the most appropriate flow for given criteria.

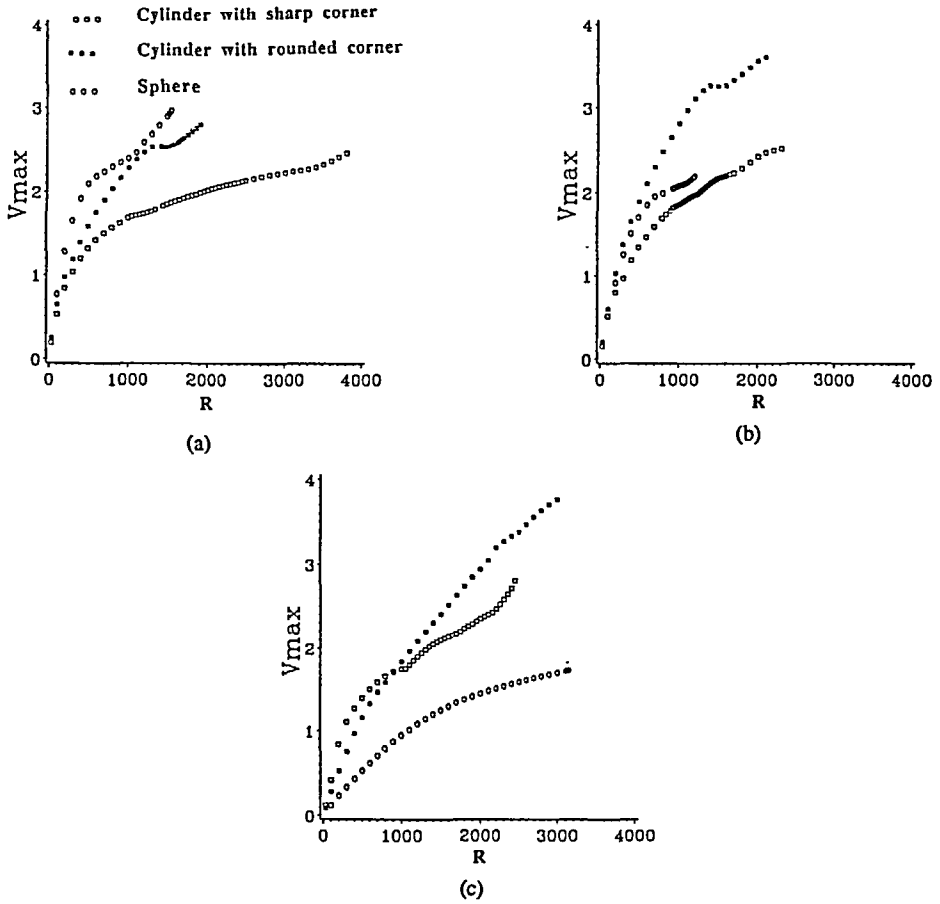

Figure 12 Maximum velocity *versus* R showing the effect of the different geometries. (a) For $R_\omega = 30$, (b) for $R_\omega = 100$ and (c) for $R_\omega = 800$

Table 3 Comparison of the logarithm of the mixing index for the various parameters and geometries considered

	$R_\omega = 30$			$R_\omega = 100$			$R_\omega = 800$		
R	Sharp corner	Round corner	Sphere	Sharp corner	Round corner	Sphere	Sharp corner	Round corner	Sphere
100	−1.78	−1.71	−3.75	−3.26	−2.55	−4.06	−2.14	−2.90	−2.45
800	−2.46	−2.45	−2.29	−3.36	−3.74	−3.74	−2.86	−3.34	−4.36
1197						−3.16			
1560			−0.55						
1600	−2.66	−3.26		−4.34	−4.18		−2.74	−3.05	−3.63

Since $R_\omega/R_m = \omega L/V_0$ we can choose V_{max} for V_0 to yield a minimum of this ratio. Now, since V_{max} is always of the order unity, the initial assumption that $R_\omega \gg R_m$ can readily be enforced by choosing $\omega L \gg 1$.

To investigate the mixing of the resultant flow, the tracer dispersion problem was solved for various combinations of R_ω and R. The results are shown in *Table 3*. At $R_\omega = 30$, the sphere

is best at low R but worst at high R. For $R_\omega = 100$ the sphere is again best at low R and worst at high R. However, for $R_\omega = 800$, the sphere is markedly better than the other two for R large. One can also see that while the MI's for the cylinder and the cylinder with a rounded corner are similar at $R_\omega = 30$ and 100, at $R_\omega = 800$ the rounded corner cylinder gains a distinct edge over the plain cylinder.

CONCLUSIONS

The finite element method has successfully been used to model the stirring induced by an alternating magnetic field. The quality of stirring from the resulting flow has also been examined.

The results from the flow in a closed cylindrical crucible with sharp corners and of a closed cylindrical crucible with rounded corners show the following distinct trends: (1) regarding the Lorentz force, the maximum force decreases with increasing corner radius; (2) regarding sizes of vortices, the end vortex decreases in size for increasing R, the end vortex decreases in size for increasing R_ω and the end vortex increases in size for greater corner radius; (3) regarding strengths of vortices (maximum absolute value of stream function), both vortices increase in strength for increasing R, the end vortex decreases in strength for increasing R_ω, the equatorial vortex reaches a maximum strength for increasing R_ω and then decreases in strength, the end vortex increases in strength for greater corner radius and the equatorial vortex decreases in strength for greater corner radius.

The non-geometrical trends noted here are in total agreement with those of previous workers[13,16,18].

In examining the mixing which results from the various cases considered, $R_\omega = 100$ gives better mixing than the other values of R_ω for the cylinder with sharp corners and the cylinder with a rounded corner. This could be related to the fact that the equatorial vortex has a greater strength at $R_\omega = 100$ and being the larger in size it thus dominates in the determination of the mixing index. The rounding of the corner of the cylinder only gives a definite improvement of mixing at $R_\omega = 800$ despite the fact that the equatorial vortex is weaker.

In similar work to this, where quantifying mixing has been attempted, the norm seems to be to define a mixing time which is usually defined to be the time taken for the concentration at a given location to continuously fall within 5% of the final, well mixed concentration[7,8]. Naturally, it is preferable to look at the entire field as opposed to one particular location, but the latter approach is more readily applicable to experimental work. In numerical work it is obviously very easy to look at the entire field as has been done in this work. We could thus have compared mixing times by defining this as the time taken for the mixing index to drop below say 0.01 or some other suitable value.

However, the problem of in which element to concentrate the tracer initially still remains an open question. We found that $R_\omega = 30$ gave the smallest deviation in the mixing index for different initial locations of the tracer for all the values of R investigated. For $R_\omega = 100$ and 800, the mixing index varied by as much as an order of magnitude, for a given value of R. It would probably be best to solve the tracer dispersion problem with several different initial locations and then take an average. Alternatively, one could look at the worst mixing index out of the several chosen. The way of deciding this would have to be such so that the results would agree with practice.

In conclusion, the following recommendations can be made.

Regarding the numerical modelling of this type of problem, various extensions could be considered from the host of models already investigated using finite differences. These could include a finite length coil, a turbulence flow model and/or a free surface model. Concerning the mixing, it might be better to investigate it in terms of a mixing time, defined as the time taken for the mixing index to fall below a certain value, as opposed to comparing the mixing indices after a fixed time as was done here. The problem of where to locate the initial tracer concentration could also be investigated.

Regarding the practical implications of this work, it is clear that designers of such systems could use the rounding of the corner as a means of improving the mixing. The rounding of the corner has already been done because of the corrosion in the corner, but the amount of rounding could be chosen to optimize the mixing. In conjunction with this, designers could search for the optimum values of R_ω and R for their particular application.

ACKOWLEDGEMENTS

The assistance of Prof. A. Solan is greatefully acknowledged.

This research was supported by the Y. Winograd Chair of Fluid Mechanics and Heat Transfer at Technion.

This work was carried out on the Convex C-220 at the Technion.

REFERENCES

1 Murthy, A. and Szekely, J. Some fundamental aspects of mixing in metallurgical reaction systems, *Metall Trans.*, **17B**, 487–490 (1986)
2 Mazumdar, D. and Guthrie, R. I. L. Mixing models for gas stirred metallurgical reactors, *Metall. Trans.*, **17B**, 725–733 (1986)
3 Murthey, G. G., Krishna, G. A. and Mohrotra, S. P. Mathematical modeling of mixing phenomena in a gas stirred liquid bath, *Metall. Trans.* **20B**, 53–59 (1989)
4 Sahai, Y. Fluid dynamics in channel reactors stirred by submerged gas injection, *Metall. Trans.*, **19B**, 603–612 (1988)
5 Szekely, J., Wang, H. J. and Kiser, K. M. Flow pattern velocity and turbulence energy measurement and predictions in a water model of an argon-stirred ladle, *Metall. Trans.* **7B**, 287–295 (1976)
6 Sinha, U. P. and McNallan, M. J. Mixing in ladles by vertical injection of gas and gas-particle jets—a water model study, *Metall. Trans.*, **16B**, 850–853 (1985)
7 Nakanishi, K., Szekely, J., Fujii, T., Mihara, Y. and Iwaoka, S. Stirring and its effect on aluminium deoxidation of steel in the ASEA–SKF furnace: Part I. Plant scale measurements and preliminary analysis, *Metall. Trans.* **6B**, 111–118 (1975)
8 Szekely, J. and Nakanishi, K. Stirring and its effect on aluminium deoxidation of steel in the ASEA–SKF furnace: Part II. Mathematical representation of the turbulent flow field and of tracer dispersion, *Metall. Trans.*, **6B**, 245–256 (1975)
9 Moffat, H. K. On fluid flow induced by a rotating magnetic field, *J. Fluid Mech.*, **22**, 521–528 (1965)
10 Sneyd, A. Generation of fluid motion in a circular cylinder by an unsteady applied magnetic field, *J. Fluid Mech.*, **49**, 817–829 (1971)
11 Davidson, P. A., Hunt, J. C. R. and Moros, A. Turbulent recirculating flows in liquid-metal MHD, in *Liquid Metal Flows: Magnetohydrodynamics and Applications* (Eds. H. Branover, M. Mond and Y. Unger), *Progr. Astronaut. Aeronaut.*, **111**, pp. 400–420, AIAA, Washington DC (1988)
12 Szekely, J., Chang, C. W. and Ryan, R. E. The measurement and prediction of the melt velocities in a turbulent, electromagnetically driven recirculating low melting alloy system, *Metall. Trans.*, **8B**, 333–338 (1977)
13 Cremer, P. and Driole, J. Effects of the electromagnetic stirring on the removal of inclusions of oxide from liquid steel, *Metall. Trans.* **13B**, 45–52 (1982)
14 Taberlet, E. and Fautrelle, Y. R. Investigation of the turbulent flow in an induction furnace supplied with various frequencies, *Single- and Multi-Phase Flows in an Electromagnetic Field, Energy, Metallurgical, and Solar Applications* (Eds. Branover, H., Lykoudis, P. S., Mond, M.), *Progr. Astronaut. Aeronaut.*, **100**, pp. 593–616, AIAA, New York (1985)
15 Taberlet, E. and Fautrelle, Y. R. Turbulent stirring in an experimental induction furnace, *J. Fluid Mech.*, **159**, 409–431 (1985)
16 El-Kaddah, N. Szekely, J., Taberlet, E. and Fautrelle, Y. Turbulent recirculating flow in induction furnaces: a comparison of measurement with predictions over a range of operating conditions, *Metall. Trans.* **17B**, 687–693 (1986)
17 Meyer, J. L., El-Kaddah, N. Szekely, J., Vives, C. and Ricou, R. A comprehensive study of the induced current, the electromagnetic force field, and the velocity field in a complex electromagnetically driven flow system, *Metall. Trans.* **18B**, 529–538 (1987)
18 Fautrelle, Y. R. Analytical and numerical aspects of the electromagnetic stirring induced by alternating magnetic fields, *J. Fluid Mech.*, **102**, 405–430 (1981)
19 Barbier, J. N., Fautrelle, Y. R., Evans, J. W. and Cremer, P. Simulation numerique der fours chauffes par induction, *J. Mecan. Appl.*, **1**, 533–556 (1982)
20 Wu, S. T. Unsteady MHD duct flow by the finite element method, *Int. J. Num. Meth. Eng.*, **6**, 3–10 (1973)
21 Singh, B. and Lal, J. Effect of magnetic field orientation and wall conductivity on MHD channel flows using finite element method, *Comp. Meth. Appl. Mech. Eng.*, **40**, 159–170 (1983)

22 Winowich, N. S. Magnetohydrodynamic channel flow with a nonuniform magnetic field and conductive walls, *PhD Thesis*, Carnegie-Mellon University (1986)
23 Shercliff, J. A. *A Textbook of Magnetohydrodynamics*, Pergamon Press, Oxford, p. 24 (1965)
24 Roberts, P. H. *An Introduction to Magnetohydrodynamics*, Longmans, London, p. 58, (1967)
25 Berelowitz, M. The finite element analysis of stirring induced by alternating magnetic fields, *M.sc Thesis*, Technion—Israel Institute of Technology (in English) (1990)
26 Moreau, R. MHD flows driven by alternating magnetic field, *MHD-Flow and Turbulence II* (Eds. H. Branover, A. Yakhot), Israel Universities Press, Jerusalem (1980)
27 Gunzburger, M. D. *Finite Element Methods for Viscous Incompressible flows: A Guide to Theory, Practice, and Algorithms*, Academic Press, San Diego, p. 72 (1989)
28 Hood, P. frontal solution program for unsymmetric matrices, *Int. J. Num. Meth. Eng.*, **10**, 379–399 (1976)
29 Zienkiewicz, O. C. *The Finite Element Method*, 3rd Edn, McGraw-Hill Book Company, London, p. 633 (1977)

APPENDIX: VALUES OF STREAMFUNCTIONS ON GRAPHS

Legend	Streamfunction value	Legend	Streamfunction value
A	−0.24	P	0.00
B	−0.20	Q	0.006
C	−0.18	R	0.012
D	−0.16	S	0.018
E	−0.14	T	0.02
F	−0.12	U	0.024
G	−0.10	V	0.03
H	−0.08	W	0.04
I	−0.06	X	0.06
J	−0.04	Y	0.08
K	−0.024	Z	0.10
L	−0.02	ZA	0.12
M	−0.018	ZB	0.16
N	−0.012	ZC	0.20
O	−0.006		